Article

Linear-in-temperature resistivity for optimally superconducting (Nd,Sr)NiO_2

https://doi.org/10.1038/s41586-023-06129-x

Received: 3 March 2022

Accepted: 25 April 2023

Published online: 12 July 2023

Check for updates

Kyuho Lee[1,2]✉, Bai Yang Wang[1,2], Motoki Osada[1,3], Berit H. Goodge[4,5], Tiffany C. Wang[1,6], Yonghun Lee[1,6], Shannon Harvey[1,6], Woo Jin Kim[1,6], Yijun Yu[1,6], Chaitanya Murthy[2], Srinivas Raghu[1,2], Lena F. Kourkoutis[4,5] & Harold Y. Hwang[1,6]

The occurrence of superconductivity in proximity to various strongly correlated phases of matter has drawn extensive focus on their normal state properties, to develop an understanding of the state from which superconductivity emerges[1–4]. The recent finding of superconductivity in layered nickelates raises similar interests[5–8]. However, transport measurements of doped infinite-layer nickelate thin films have been hampered by materials limitations of these metastable compounds: in particular, a high density of extended defects[9–11]. Here, by moving to a substrate $(LaAlO_3)_{0.3}(Sr_2TaAlO_6)_{0.7}$ that better stabilizes the growth and reduction conditions, we can synthesize the doping series of $Nd_{1-x}Sr_xNiO_2$ essentially free from extended defects. In their absence, the normal state resistivity shows a low-temperature upturn in the underdoped regime, linear behaviour near optimal doping and quadratic temperature dependence for overdoping. This is phenomenologically similar to the copper oxides[2,12] despite key distinctions—namely, the absence of an insulating parent compound[5,6,9,10], multiband electronic structure[13,14] and a Mott–Hubbard orbital alignment rather than the charge-transfer insulator of the copper oxides[15,16]. We further observe an enhancement of superconductivity, both in terms of transition temperature and range of doping. These results indicate a convergence in the electronic properties of both superconducting families as the scale of disorder in the nickelates is reduced.

The idea that superconductivity can arise from doping a correlated insulator has been a pervasive guiding principle since the discovery of the copper oxide superconductors, with an impact on materials as far-ranging as twisted bilayer graphene[1–3]. On doping the insulator, a 'strange metal' with unconventional electrical transport often occurs and nucleates superconductivity, before further doping gives way to more conventional Fermi-liquid-like behaviour. The extent to which this phenomenology requires that the parent compound shows a strongly insulating ground state, and whether or not it should show magnetism has been discussed for decades. A further dichotomy, whether the strange metallic behaviour reflects the proximity to the correlated insulator or follows from a zero-temperature phase transition to a broken symmetry phase, remains actively debated and largely unresolved.

The observation of superconductivity in a family of layered nickelates presents an opportunity to address some of these perplexing issues. The parent compounds of the infinite-layer nickelates show a weak resistive upturn at low temperatures without a strongly insulating ground state or indications of a gap ($NdNiO_2$ and $PrNiO_2$), and even evidence of superconductivity in $LaNiO_2$ (refs. 5,6,9,10). Moreover, so far, long-range magnetic order has not been observed in this system[17–19]. Nevertheless, upon doping, we find that $Nd_{1-x}Sr_xNiO_2$ shows strange metal behaviour with resistivity linearly increasing with temperature T for Sr doping x at the peak of the superconducting dome. Further hole doping results in a metallic state with resistivity varying as T^2, with reduced and ultimately vanishing superconducting scales. Our results indicate, therefore, that much of the emergent behaviour of this class of unconventional superconductors does not strictly require a Mott insulating parent compound with a hard gap to charge excitations. Features in the Hall effect directly correlate with the evolution of the resistivity and may suggest a broken symmetry associated with Fermi surface reconstruction[2,20,21]. Our results can be considered in two contexts: the multiband nature of the electronic structure[13,14,21] and the possibility of a quantum phase transition underlying the strange metallic behaviour[2,4].

Materials advances

A central issue for the synthesis and study of superconducting infinite-layer nickelates is material control due to the poor thermodynamic stability of this system[9–11], as evident from the orders-of-magnitude variations in the resistivity of infinite-layer nickelates reported across the literature[9,10,22–25]. Just as in the development of copper oxides[1,26,27], minimizing disorder and extrinsic defects is critical for elucidating the nature of the normal state and superconducting phase diagram.

[1]Stanford Institute for Materials and Energy Sciences, SLAC National Accelerator Laboratory, Menlo Park, CA, USA. [2]Department of Physics, Stanford University, Stanford, CA, USA. [3]Department of Materials Science and Engineering, Stanford University, Stanford, CA, USA. [4]School of Applied and Engineering Physics, Cornell University, Ithaca, NY, USA. [5]Kavli Institute at Cornell for Nanoscale Science, Cornell University, Ithaca, NY, USA. [6]Department of Applied Physics, Stanford University, Stanford, CA, USA. ✉e-mail: kyuho@stanford.edu

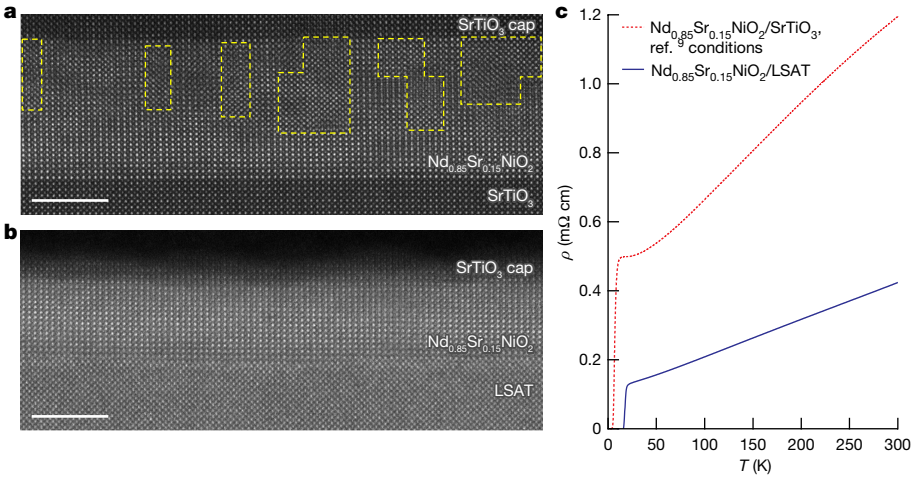

Fig. 1 | Enhanced crystallinity of $Nd_{1-x}Sr_xNiO_2$ thin films on LSAT. a, HAADF-STEM cross-sectional image of a $Nd_{0.85}Sr_{0.15}NiO_2$ thin film grown on $SrTiO_3$, synthesized using conditions in ref. 9. Regions bounded by Ruddlesden–Popper-type stacking faults are outlined in yellow dashed lines. The half-unit-cell displacement induced by the stacking fault inclusions blurs the cation contrast[11,28], making the regions with stacking faults easily distinguishable from the pristine infinite-layer (Extended Data Fig. 1a). **b**, HAADF-STEM cross-sectional image of a $Nd_{0.85}Sr_{0.15}NiO_2$ thin film grown on LSAT, synthesized using the conditions specified in Extended Data Table 1. The film now displays highly uniform crystallinity largely free from extended defects. **c**, Resistivity ρ versus temperature T for the films in **a** (red dotted curve) and **b** (blue solid curve). A substantial decrease in the normal state resistivity reflects the crystallinity improvement. Scale bars, 5 nm.

We have achieved substantial advances in the crystallinity of $Nd_{1-x}Sr_xNiO_2$ ($x = 0.05–0.325$) by using $(LaAlO_3)_{0.3}(Sr_2TaAlO_6)_{0.7}$ (LSAT; lattice constant $a = 3.868$ Å) substrates to optimize the epitaxial mismatch for both the perovskite precursor and the infinite-layer phases (Extended Data Table 1; see Supplementary Information for an extended comparison of LSAT and $SrTiO_3$). We note that the use of LSAT substrates and the enhancement of the superconducting onset transition temperature T_c was first reported by ref. 24 for $Pr_{0.8}Sr_{0.2}NiO_2$. As shown in the high-angle annular dark-field (HAADF)–scanning transmission electron microscopy (STEM) cross-sectional images (Fig. 1a,b), the Ruddlesden–Popper-type vertical stacking faults[9,11,28] (marked by yellow dashed outlines in Fig. 1a) that densely populate films grown on the widely used substrate $SrTiO_3$ ($a = 3.905$ Å) are now essentially eliminated on LSAT, leaving a macroscopically clean thin film with minimal defects (Fig. 1b and Extended Data Figs. 1 and 2). This is also reflected in the substantial decrease in resistivity ρ (Fig. 1c). Note that the in-plane lattice constants of the films are locked to the substrate in both cases (Fig. 1a,b and Extended Data Fig. 3d–g). X-ray diffraction θ–2θ symmetric scans show prominent film peaks with out-of-plane lattice constant trends associated with systematic Sr doping (Extended Data Fig. 3a–c). Overall, these data indicate that high crystallinity is uniformly established throughout the probed range of Sr doping (Extended Data Figs. 3 and 4), minimizing extended-defect contributions to electrical transport.

Superconducting dome

This optimized sample series on LSAT provides a robust platform to investigate the phase diagram of the infinite-layer nickelates. We first observe that ρ(20 K) now maintains a similar range of 0.1–0.3 mΩ cm across all x, notably below the scale of a resistance quantum R_q per NiO_2 plane (Fig. 2a; see Extended Data Fig. 5 for all individual $\rho(T)$ curves). This includes the underdoped and overdoped regimes, with ρ(20 K) roughly 5–30 times lower than any previously reported (roughly 0.6–9 mΩ cm)[5,9–11]. This suggests that the low-temperature normal state scattering rate is comparable across the phase diagram, although multiband effects should be considered.

It is noteworthy that a superconducting dome is still observed for films on LSAT (Fig. 2b–d and Extended Data Table 2). For previous films on $SrTiO_3$, a direct correlation was found between the presence of superconductivity and the magnitude of the normal state resistance with respect to R_q (refs. 6,9). The fact that the normal state resistance depends substantially on the substrate (LSAT versus $SrTiO_3$), whereas the existence of the superconducting dome does not, suggests that the dome itself is not a result of disorder in doped nickelates. However, at a quantitative level, the superconducting dome in the lower resistance films on LSAT is notably larger, with T_c above 20 K for optimal doping at $x \cong 0.15–0.175$ (Fig. 2b), and with a width $\Delta x \cong 0.2$ that is now very comparable to that of the copper oxides ($\Delta x \cong 0.21$ for $La_{2-x}Sr_xCuO_4$)[12] (Extended Data Fig. 6). Further data (field suppression of superconductivity and mutual-inductance measurements) for optimal doping are given in Extended Data Fig. 7. We also note that the experimentally observed range of the superconducting dome here shows good agreement with the theoretical calculations in ref. 29. Both the robustness of the dome and the higher T_c indicate that superconductivity here is probably unconventional and cannot be explained purely by electron–phonon mechanisms[30].

Normal state phase diagram

Figure 2b shows the variation of the slope of $\rho(T)$ normalized to the room-temperature value across the phase diagram. Three regimes of behaviour are observed, with representative data shown in Fig. 2e–g: a resistive upturn in the underdoped region characterized by T_{upturn} (the temperature at which the resistivity minimum occurs ($d\rho/dT = 0$)), $\rho \propto T^2$ in the overdoped region, and a narrow range of $\rho \propto T$ at the peak of the superconducting dome.

The evolution of the resistivity is accompanied by systematic features in the Hall coefficient R_H. At high temperatures and low doping R_H is negative, whereas it is positive in the low-temperature limit beyond optimal doping (Fig. 2c; see Extended Data Fig. 8 for all individual $R_H(T)$ curves). The boundary defining the sign change in R_H extrapolates to $T = 0$ at optimal doping. The second clear feature in R_H can be seen in the underdoped region. Here, R_H is negative at all temperatures and shows a pronounced local maximum (Fig. 2d). The temperature at which this maximum occurs decreases as a function of doping and tracks the resistive upturn (dark-blue triangles in Fig. 2b), such that both features extrapolate to vanish under the peak of the superconducting dome.

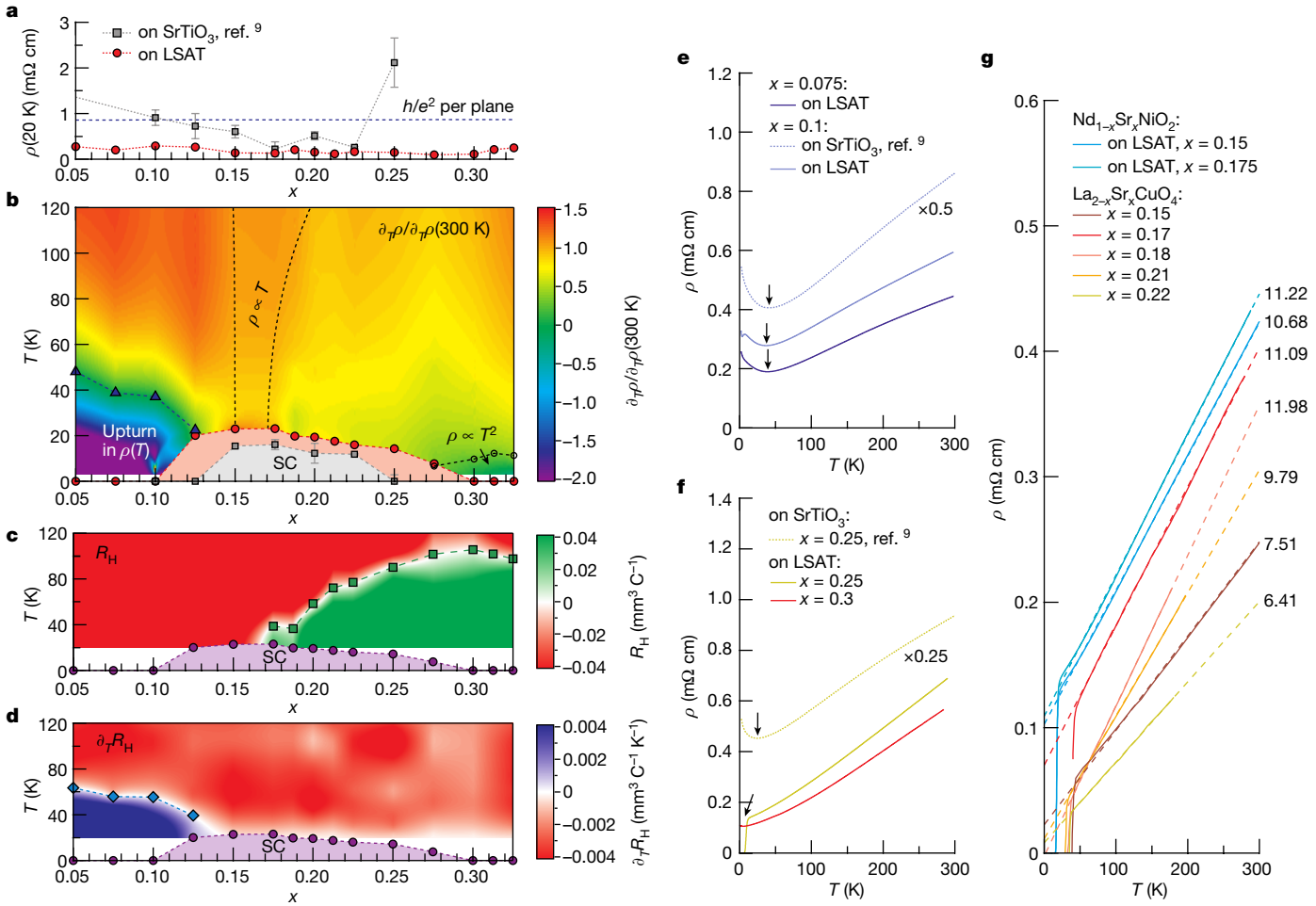

Fig. 2 | Phase diagram of highly crystalline $Nd_{1-x}Sr_xNiO_2$. a, ρ(20 K) versus x for $Nd_{1-x}Sr_xNiO_2$ films on $SrTiO_3$ (ref. 9, grey squares) and on LSAT (red circles). The LSAT samples uniformly show low ρ(20 K) well below the quantum of resistance per NiO_2 plane for all x. **b**, Contour plot of the slope of $\rho(T)$ ($\partial_T\rho$) normalized by the slope at room temperature for the films on LSAT. The superconducting dome for the films on $SrTiO_3$ (ref. 9) (grey squares) and here on LSAT (red circles) are also depicted, with the onset transition temperature $T_{c,onset}$ defined as the temperature at which the second derivative of $\rho(T)$ becomes negative. The boundary at which $\partial_T\rho$ is roughly equal to the room-temperature slope (that is, linear resistivity) is marked by black dotted lines. The temperature dependence of ρ in the underdoped, optimal and overdoped regions are labelled. The dark-blue triangles in the underdoped region mark where $\partial_T\rho = 0$ (T_{upturn}), and the open circles in the overdoped region mark the temperatures at which the T^2 fit deviates (grey arrows in Fig. 4). **c**,**d**, Contour plots of the Hall coefficient $R_H(T)$ (**c**) and the slope of $R_H(T)$ ($\partial_T R_H$) (**d**) across the superconducting dome (purple circles). The green squares in **c** show where R_H crosses zero, and the blue diamonds in **d** indicate the temperature at which the local extremum of $R_H(T)$ occurs. For **b**–**d**, the contours were interpolated from the data using natural neighbour interpolation. In **a**,**b**, the error bars are the standard deviation of 3–4 samples. **e**–**g**, $\rho(T)$ at representative x characteristic of the underdoped (**e**), overdoped (**f**) and optimally doped (**g**) regions. Dotted curves are for the films grown on $SrTiO_3$ (ref. 9), whereas solid curves are the optimized films grown on LSAT. Black arrows in **e** and **f** indicate T_{upturn}. For **g**, $\rho(T)$ of single-crystal $La_{2-x}Sr_xCuO_4$ with T-linear normal state ρ are also plotted for comparison[36,37,41]. The dashed lines are linear fits to the normal state ρ, with the slopes of the linear fit indicated at the right in units of 10^{-4} mΩ cm K^{-1}.

Underdoped regime

In the underdoped region, the low-temperature resistivity has been noted to vary as roughly log(1/T) for films on $SrTiO_3$ (ref. 31). Comparing data for films on LSAT, we see that although the resistivity itself is a factor of around four smaller in the cleaner samples, T_{upturn} is nearly the same (Fig. 2e). T_{upturn} is also essentially constant as a function of magnetic field, with an overall relatively small magnetoresistance (Fig. 3). These observations suggest that the resistive upturn cannot be directly ascribed to disorder or localization effects (with or without interaction corrections), nor to Kondo physics[32]. Indeed, by extending measurements down to lower temperatures, we observe a saturation in the resistivity below 2 K (Fig. 3).

Both the resistive upturn and ultimate saturation are closely tracked by $R_H(T)$, with identical functional form (Fig. 3). This behaviour is naturally and most simply explained within a two-band model with both electron and hole carriers. Electronic structure calculations for the nickelates indicate the presence of a large hole pocket with $3d_{x^2-y^2}$ character, and electron pockets arising from Nd 5d and Ni 3d hybridization, making this an intrinsically multiband system[13,14,21]. A two-band analysis concludes that the observed magnetotransport behaviour corresponds to a decrease in the hole carrier contribution in the presence of parallel electron conduction (Supplementary Information).

The relative insensitivity of T_{upturn} to disorder strength (Fig. 2e) further suggests that the upturn is caused by strong correlation effects that effectively freeze out the hole contribution to conduction. The recent observations of charge order in infinite-layer nickelates with an incommensurate wave vector of roughly (1/3, 0) reciprocal lattice units[33–35] provide a candidate for the correlations driving the upturn. This would also be consistent with the lack of magnetic field dependence of T_{upturn}. Notably, the upturn in resistivity—with T_{upturn} decreasing as a function of x—and the presence of strong correlation effects are

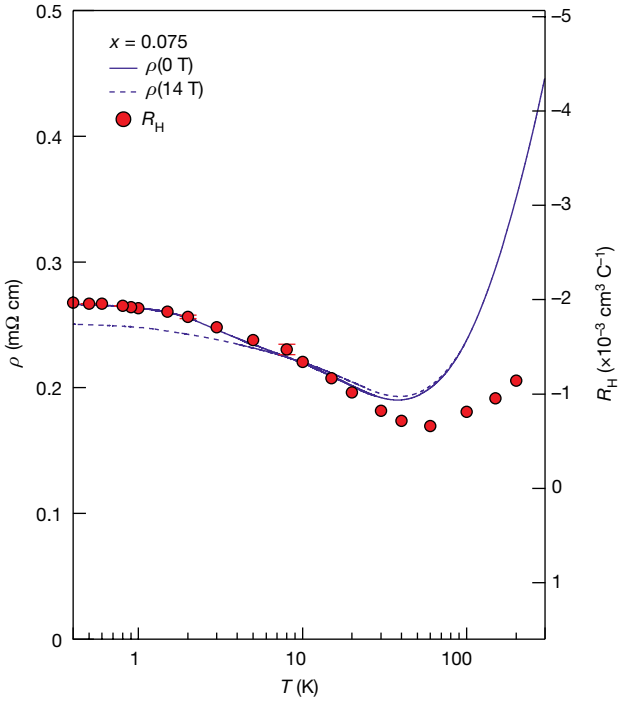

Fig. 3 | Magnetotransport characteristics of the underdoped regime. Temperature dependence of ρ (left, at 0 and 14 T) and R_H (right, note the reverse vertical scale) for $x = 0.075$. The functional form of ρ and R_H converges as the resistive upturn onsets at lower temperatures. At $T < 5$ K, ρ deviates from a roughly $\log(1/T)$ upturn and saturates instead, with the saturation also observed in R_H.

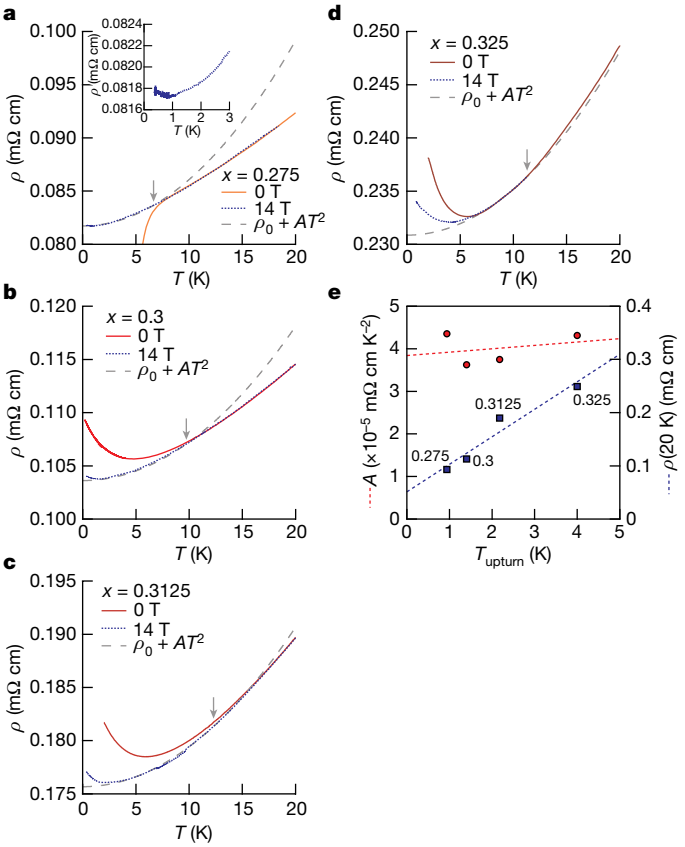

Fig. 4 | Magnetotransport characteristics of the overdoped regime. **a**–**d**, ρ versus T for overdoped $Nd_{1-x}Sr_xNiO_2$ films, with $x = 0.275$ (**a**), $x = 0.3$ (**b**), $x = 0.3125$ (**c**) and $x = 0.325$ (**d**). Solid curves are measured at zero magnetic field and dotted blue curves are measured under 14 T applied magnetic field. The $\rho_0 + AT^2$ quadratic fits are shown as dashed grey curves. The grey arrows indicate the temperature at which the quadratic fit deviates. The inset in **a** shows a magnified view of the small resistive upturn at $T < 1$ K under 14 T applied magnetic field. **e**, Quadratic fit parameter A (left, red circles) and $\rho(20\ \text{K})$ (right, blue squares) versus T_{upturn} at 14 T for the four films in **a**–**d**, with linear fits shown as dashed lines and x labelled. A shows minimal correlation with T_{upturn} and $\rho(20\ \text{K})$ shows a strong linear trend with T_{upturn}.

highly reminiscent of the underdoped region of the copper oxide phase diagram (Extended Data Fig. 6)[2,12,36,37].

Overdoped regime

In contrast to the underdoped regime, the temperature onset of the resistive upturn in the overdoped region is considerably reduced when lowering disorder (Fig. 2f) and under applied magnetic field (Fig. 4a–d). Indeed, T_{upturn} shows a strong linear correlation with the low-temperature normal state resistivity (Fig. 4e). We also note that the suppression of resistive upturn shows minimal dependence on epitaxial strain (Extended Data Fig. 9). These observations indicate that the resistive upturn in the overdoped region is driven by disorder physics, unlike in the underdoped region where, as we have discussed, it appears to arise from correlation effects. Suppressing the upturn (or superconductivity) with a 14 T magnetic field reveals metallic Fermi-liquid-like $\rho \cong AT^2$ at low temperatures, with the quadratic coefficient A essentially uncorrelated with T_{upturn} or x (Fig. 4e). In addition, the temperature at which the measured resistivity starts to deviate from the low-temperature T^2 fit increases as a function of x (Fig. 4a–d), in a manner analogous to the crossover in the functional form of ρ from $T + T^2$ or T^n $(1 < n < 2)$ to T^2 in the overdoped region of the copper oxide phase diagram[2,38]. Furthermore, $R_H(T)$ rather resembles that in overdoped $La_{2-x}Sr_xCuO_4$ in terms of magnitude, functional form and a sign change at around 100 K (ref. 39).

T-linear resistivity at optimal doping

A notable feature that emerges for the highly crystalline films on LSAT is the strange metallic $\rho \propto T$ behaviour in the normal state near optimal doping of $x \cong 0.15$–0.175 (Fig. 2b,g). The evolution of the functional form and the emergence of T-linear behaviour with reduced disorder (Fig. 1c) are similarly observed in disorder studies of the copper oxides[40]. The T-linear slope of the infinite-layer nickelates (roughly 11 mΩ cm K^{-1}) is also close to that of $La_{2-x}Sr_xCuO_4$ (roughly 6–11 mΩ cm K^{-1}) (Fig. 2g)[36,37,41]. Among the copper oxides, this comparison appears most apt given that both systems share the solid-solution cation disorder associated with chemical hole doping. The T-linear resistivity in copper oxides has been a longstanding puzzle, and it is one of several examples that have raised consideration of fundamental bounds on scattering rates[42]. For the nickelates, the lack of experimental measures of the multiband effective masses and carrier densities preclude attempts at a quantitative analysis. However, it is surprising that the value of the nickelate T-linear slope itself is so close to that of $La_{2-x}Sr_xCuO_4$ despite the notable differences in the electronic structure that result in parallel conduction channels. Whereas the ultimate origins of strange metallicity (and the upturn in resistance on the underdoped side) are yet unclear, the observations here directly indicate that a parent compound with a hard insulating gap is not a crucial ingredient for the strange metal physics that ensues near optimal doping for superconductivity.

Discussion

If strange metallicity is not directly tied to a proximate Mott insulator, a commonly invoked alternative would involve scattering off the soft

order parameter fluctuations associated with a continuous quantum phase transition occluded by the superconducting dome[2,4]. Further studies are needed to determine the nature of such fluctuations if present—the charge stripe phase is a plausible candidate[33–35]—and their effect on the resistive upturn in the underdoped regime. When all of the magnetotransport features are summarized on a common phase diagram (Extended Data Fig. 10), it is suggestive of such a quantum critical scenario: the monotonic decrease of the resistive T_{upturn} (and associated R_H maximum) with doping and its apparent vanishing near optimal doping, and Hall measurements that mark a locus of doping dependent temperatures on the overdoped side in which the effective sign of the carriers changes, which again vanishes approaching optimal doping. These features have been presented in a two-band picture appropriate for the nickelates, and strictly within this framework the evolution of R_H could be coincidental, reflecting the details of the underlying fermiology of the material: there are analogous debates on multiband effects in the copper oxides, for both hole and electron doping[20]. Alternatively, the vanishing Hall number could be ascribed to Fermi surface reconstruction associated with a density wave order parameter for both nickelates and copper oxides, and thus of more fundamental significance.

With a resistive upturn in the underdoped region driven by strong electron correlations, a non-Fermi-liquid T-linear resistivity near optimal doping and T^2 resistivity in the overdoped region, the superconducting phase diagram of the infinite-layer nickelates bears a close resemblance to that of $La_{2-x}Sr_xCuO_4$ (Extended Data Fig. 10). This is surprising, especially considering the key distinctions between the two systems. The undoped parent state of the nickelates is not an antiferromagnetic insulator[6,9,10,17–19]. The hybridization between the Nd 5*d* and Ni 3*d* bands introduces electron pockets in the Fermi surface, making the nickelates an intrinsically multiband system[13,14,21]. Spectroscopic measurements suggest that the orbital alignment of the nickelates is closer to the Mott–Hubbard regime, rather than the charge-transfer regime such as the hole-doped copper oxides[15,16]. And yet, the $Nd_{1-x}Sr_xNiO_2$ phase diagram—in particular the superconducting dome and the electrical transport in the normal state—is similar to that of $La_{2-x}Sr_xCuO_4$. The good agreement in the superconducting dome with calculations assuming pairing predominantly in the Ni $3d_{x^2-y^2}$ band[29] suggests that the same mechanism could be at play in both systems. Similarities in the phase diagram extend beyond these oxides to materials as disparate as twisted bilayer graphene and chalcogenides[3,4], hinting at an underlying universality in their electrical transport that remains to be understood.

Online content

Any methods, additional references, Nature Portfolio reporting summaries, source data, extended data, supplementary information, acknowledgements, peer review information; details of author contributions and competing interests; and statements of data and code availability are available at https://doi.org/10.1038/s41586-023-06129-x.

1. Lee, P. A., Nagaosa, N. & Wen, X. G. Doping a Mott insulator: physics of high-temperature superconductivity. *Rev. Mod. Phys.* **78**, 17–85 (2006).
2. Keimer, B., Kivelson, S. A., Norman, M. R., Uchida, S. & Zaanen, J. From quantum matter to high-temperature superconductivity in copper oxides. *Nature* **518**, 179–186 (2015).
3. Cao, Y. et al. Unconventional superconductivity in magic-angle graphene superlattices. *Nature* **556**, 43–50 (2018).
4. Fernandes, R. M. et al. Iron pnictides and chalcogenides: a new paradigm for superconductivity. *Nature* **601**, 35–44 (2022).
5. Li, D. et al. Superconductivity in an infinite-layer nickelate. *Nature* **572**, 624–627 (2019).
6. Osada, M. et al. Nickelate superconductivity without rare-earth magnetism: $(La,Sr)NiO_2$. *Adv. Mater.* **2021**, 2104083 (2021).
7. Pan, G. A. et al. Superconductivity in a quintuple-layer square-planar nickelate. *Nat. Mater.* **21**, 160–164 (2022).
8. Zeng, S. et al. Superconductivity in infinite-layer nickelate $La_{1-x}Ca_xNiO_2$ thin films. *Sci. Adv.* **8**, eabl9927 (2022).
9. Li, D. et al. Superconducting dome in $Nd_{1-x}Sr_xNiO_2$ infinite layer films. *Phys. Rev. Lett.* **125**, 027001 (2020).
10. Zeng, S. et al. Phase diagram and superconducting dome of infinite-layer $Nd_{1-x}Sr_xNiO_2$ thin films. *Phys. Rev. Lett.* **125**, 147003 (2020).
11. Lee, K. et al. Aspects of the synthesis of thin film superconducting infinite-layer nickelates. *APL Mater.* **8**, 041107 (2020).
12. Takagi, H. et al. Superconductor-to-nonsuperconductor transition in $(La_{1-x}Sr_x)_2CuO_4$ as investigated by transport and magnetic measurements. *Phys. Rev. B* **40**, 2254–2261 (1989).
13. Lee, K. W. & Pickett, W. E. Infinite-layer $LaNiO_2$: Ni^{1+} is not Cu^{2+}. *Phys. Rev. B* **70**, 165109 (2004).
14. Botana, A. S. & Norman, M. R. Similarities and differences between $LaNiO_2$ and $CaCuO_2$ and implications for superconductivity. *Phys. Rev. X* **10**, 011024 (2020).
15. Hepting, M. et al. Electronic structure of the parent compound of superconducting infinite-layer nickelates. *Nat. Mater.* **19**, 381–385 (2020).
16. Goodge, B. H. et al. Doping evolution of the Mott-Hubbard landscape in infinite-layer nickelates. *Proc. Natl Acad. Sci. USA* **118**, e2007683118 (2021).
17. Hayward, M. A., Green, M. A., Rosseinsky, M. J. & Sloan, J. Sodium hydride as a powerful reducing agent for topotactic oxide deintercalation: synthesis and characterization of the nickel(I) oxide $LaNiO_2$. *J. Am. Chem. Soc.* **121**, 8843–8854 (1999).
18. Hayward, M. A. & Rosseinsky, M. J. Synthesis of the infinite layer Ni(I) phase $NdNiO_{2+x}$ by low temperature reduction of $NdNiO_3$ with sodium hydride. *Solid State Sci.* **5**, 839–850 (2003).
19. Wang, B.-X. et al. Synthesis and characterization of bulk $Nd_{1-x}Sr_xNiO_2$ and $Nd_{1-x}Sr_xNiO_3$. *Phys. Rev. Mater.* **4**, 084409 (2020).
20. Greene, R. L., Mandal, P. R., Poniatowski, N. R. & Sarkar, T. The strange metal state of the electron-doped cuprates. *Annu. Rev. Condens. Matter Phys.* **11**, 213–229 (2020).
21. Leonov, I., Skornyakov, S. L. & Savrasov, S. Y. Lifshitz transition and frustration of magnetic moments in infinite-layer $NdNiO_2$ upon hole doping. *Phys. Rev. B* **101**, 241108(R) (2020).
22. Li, Y. et al. Impact of cation stoichiometry on the crystalline structure and superconductivity in nickelates. *Front. Phys.* **9**, 719534 (2021).
23. Gao, Q., Zhao, Y., Zhou, X. J. & Zhu, Z. Preparation of superconducting thin films of infinite-layer nickelate $Nd_{0.8}Sr_{0.2}NiO_2$. *Chinese Phys. Lett.* **38**, 077401 (2021).
24. Ren, X. et al. Superconductivity in infinite-layer $Pr_{0.8}Sr_{0.2}NiO_2$ films on different substrates. Preprint at https://arxiv.org/abs/2109.05761 (2021).
25. Ding, X. et al. Stability of superconducting $Nd_{0.8}Sr_{0.2}NiO_2$ thin films. *Sci. China-Phys. Mech. Astron.* **65**, 267411 (2022).
26. Attfield, J. P., Kharlanov, A. L. & McAllister, J. A. Cation effects in doped La_2CuO_4 superconductors. *Nature* **394**, 157–159 (1998).
27. Kim, G. et al. Optical conductivity and superconductivity in highly overdoped $La_{2-x}Ca_xCuO_4$ thin films. *Proc. Natl Acad. Sci. USA* **118**, e2106170118 (2021).
28. Guo, Q., Farokhipoor, S., Magén, C., Rivadulla, F. & Noheda, B. Tunable resistivity exponents in the metallic phase of epitaxial nickelates. *Nat. Commun.* **11**, 2949 (2020).
29. Kitatani, M. et al. Nickelate superconductors—a renaissance of the one-band Hubbard model. *npj Quantum Mater.* **5**, 59 (2020).
30. Nomura, Y. et al. Formation of a two-dimensional single-component correlated electron system and band engineering in the nickelate superconductor $NdNiO_2$. *Phys. Rev. B.* **100**, 205138 (2019).
31. Zhang, G. M., Yang, Y. F. & Zhang, F. C. Self-doped Mott insulator for parent compounds of nickelate superconductors. *Phys. Rev. B.* **101**, 020501(R) (2020).
32. Hsu, Y. T. et al. Insulator-to-metal crossover near the edge of the superconducting dome in $Nd_{1-x}Sr_xNiO_2$. *Phys. Rev. Res.* **3**, L042015 (2021).
33. Rossi, M. et al. A broken translational symmetry state in an infinite-layer nickelate. *Nat. Phys.* **18**, 869–873 (2022).
34. Krieger, G. et al. Charge and spin order dichotomy in $NdNiO_2$ driven by the capping layer. *Phys. Rev. Lett.* **129**, 027002 (2022).
35. Tam, C. C. et al. Charge density waves in infinite-layer $NdNiO_2$ nickelates. *Nat. Mater.* **21**, 1116–1120 (2022).
36. Takagi, H. et al. Systematic evolution of temperature-dependent resistivity in $La_{2-x}Sr_xCuO_4$. *Phys. Rev. Lett.* **69**, 2975–2978 (1992).
37. Boebinger, G. S. et al. Insulator-to-metal crossover in the normal state of $La_{2-x}Sr_xCuO_4$ near optimum doping. *Phys. Rev. Lett.* **77**, 5417–5420 (1996).
38. Hussey, N. E. Phenomenology of the normal state in-plane transport properties of high-T_c cuprates. *J. Phys. Condens. Matter* **20**, 123201 (2008).
39. Hwang, H. Y. et al. Scaling of the temperature dependent Hall effect in $La_{2-x}Sr_xCuO_4$. *Phys. Rev. Lett.* **72**, 2636–2639 (1994).
40. Fukuzumi, Y., Mizuhashi, K., Takenaka, K. & Uchida, S. Universal superconductor-insulator transition and T_c depression in Zn-substituted high-T_c cuprates in the underdoped regime. *Phys. Rev. Lett.* **76**, 684–687 (1996).
41. Cooper, R. A. et al. Anomalous criticality in the electrical resistivity of $La_{2-x}Sr_xCuO_4$. *Science* **323**, 603–607 (2009).
42. Bruin, J. A. N., Sakai, H., Perry, R. S. & Mackenzie, A. P. Similarity of scattering rates in metals showing T-linear resistivity. *Science* **339**, 804–807 (2013).

Methods

Film growth

Polycrystalline $Nd_{1-x}Sr_xNi_{1.15}O_3$ targets (x = 0.05–0.325) were prepared by pelletizing mixtures of Nd_2O_3, $SrCO_3$ and NiO powders, decarbonating at 1,200 °C for 12 h, regrinding and repelletizing and then sintering at 1,350 °C for 12 h (Extended Data Fig. 11)[5,11]. Roughly 15 unit cells of $Nd_{1-x}Sr_xNiO_3$ epitaxial thin films were grown by pulsed-laser deposition with a KrF excimer laser (λ = 248 nm) on 5 × 5 mm^2 LSAT (001) and $SrTiO_3$ (001) substrates, with the substrate surface prepared ex situ by standard acetone-isopropyl alcohol ultrasonication. The films were synthesized using the conditions specified in Extended Data Table 1. Roughly four unit cells of $SrTiO_3$ (001) were grown in situ as a capping layer[11].

Reduction process

After cutting into two 2.5 × 5 mm^2 pieces, the perovskite samples were vacuum-sealed (below 0.1 mTorr) with roughly 0.1 g of CaH_2 powder in a Pyrex glass tube, loosely wrapped with aluminium foil to avoid direct contact with CaH_2. The glass tube was first heated at 240–260 °C for 2 h, with a temperature ramp rate of 10 °C min^{-1}. Then, X-ray diffraction (XRD) θ–2θ symmetric scan and $\rho(T)$ measurements were performed ex situ to evaluate the degree of topotactic transition. Thirty-minute reductions at 240–260 °C and ex situ characterizations were incrementally continued until the out-of-plane lattice constant, superconducting transition temperature and residual resistivity ratio saturated, indicating complete reduction. The total reduction time across all samples was roughly 2.5–4 h.

Characterization

XRD θ–2θ symmetric scans and reciprocal space maps were measured using a monochromated Cu $K_{\alpha 1}$ source (λ = 1.5406 Å). Cross-sectional STEM specimens were prepared by a standard focused ion beam (FIB) lift-out process on a Thermo Scientific Helios G4 UX FIB. HAADF–STEM images of the specimens were acquired on an aberration-corrected Thermo Fisher Scientific Spectra 300 X-CFEG operated at 300 kV with a probe convergence semi-angle of 30 mrad and inner (outer) collection angles of 66 (200) mrad. The measurements of $\rho(H, T)$ and Hall effect were conducted in a six-point Hall bar geometry using aluminium wire-bonded contacts. The Hall effect was measured to be linear up to the highest measured magnetic field of 14 T. For two-coil mutual-inductance measurements, a pickup coil of 400 turns and lateral dimensions of roughly 0.5 × 0.5 mm^2 and a drive coil of 50 turns and lateral dimensions of roughly 0.25 × 0.25 mm^2 were made using 20 μm diameter copper wires. The leakage around the film was calibrated using a 100-nm thick aluminium film with the same lateral dimensions as the nickelate samples (2.5 × 5 mm^2)[43].

Data availability

The data that support the findings of this study are available from the corresponding author upon request.

43. Harvey, S. P. et al. Evidence for nodal superconductivity in infinite-layer nickelates. Preprint at https://arxiv.org/abs/2201.12971 (2022).
44. Zakharov, A. A., Lazarev, V. B. & Shaplygin, I. S. Interaction of lanthanide sesquioxides with copper and nickel oxide. *J. Inorg. Chem.* **29**, 454–456 (1984).
45. Aivazov, M. I., Sarkisyan, A. G., Domashnev, I. A. & Gurov, S. V. Synthesis and investigation of compositions in the cross section TiO-NiO. *Inorg. Mater.* **7**, 1389–1391 (1971).

Acknowledgements We thank S. Kivelson, T. Devereaux and M. Gabay for useful discussions. This work was supported by the US Department of Energy, Office of Basic Energy Sciences, Division of Materials Sciences and Engineering (contract no. DE-AC02-76SF00515) and the Gordon and Betty Moore Foundation's Emergent Phenomena in Quantum Systems Initiative (grant no. GBMF9072, synthesis equipment). C.M. acknowledges support by the Gordon and Betty Moore Foundation's Emergent Phenomena in Quantum Systems Initiative (grant no. GBMF8686). B.H.G. and L.F.K. acknowledge support by the Department of Defense Air Force Office of Scientific Research (grant no. FA 9550-16-1-0305) and the Packard Foundation. The XRD reciprocal space map measurements were performed at the Stanford Nano Shared Facilities (SNSF), supported by the National Science Foundation (NSF) under award no. ECCS-2026822. This work made use of a Helios FIB supported by the NSF (grant no. DMR-1539918) and the Cornell Center for Materials Research Shared Facilities, which are supported through the NSF MRSEC programme (grant no. DMR-1719875). The Thermo Fisher Spectra 300 X-CFEG was acquired with support from Platform for the Accelerated Realization, Analysis and Discovery of Interface Materials (PARADIM), an NSF MIP (grant no. DMR-2039380), and Cornell University.

Author contributions K.L. and H.Y.H. conceived the project. K.L. and Y.L. fabricated the polycrystalline targets. K.L. fabricated the perovskite thin films. M.O., Y.L. and W.J.K. performed the soft-chemistry reductions. K.L. conducted XRD characterizations. B.Y.W., T.C.W., Y.L., S.H., W.J.K. and Y.Y. performed the transport measurements. B.H.G. and L.F.K. conducted STEM measurements. K.L., B.Y.W., C.M., S.R. and H.Y.H. wrote the manuscript with input from all authors.

Competing interests The authors declare no competing interests.

Additional information

Supplementary information The online version contains supplementary material available at https://doi.org/10.1038/s41586-023-06129-x.

Correspondence and requests for materials should be addressed to Kyuho Lee.

Peer review information *Nature* thanks the anonymous reviewers for their contribution to the peer review of this work. Peer reviewer reports are available.

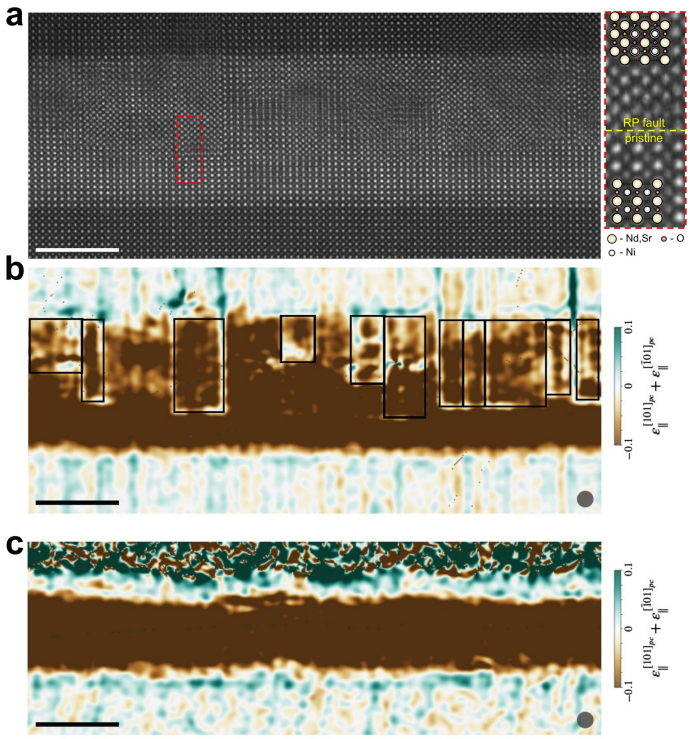

Extended Data Fig. 1 | Analytical mapping of Ruddlesden–Popper faults. **a**, Raw HAADF-STEM image of the $Nd_{0.85}Sr_{0.15}NiO_2$ film on $SrTiO_3$ substrate shown in Fig. 1a (left) and a magnified view of the region marked by the red dashed box (right). For the magnified view, atomic overlays are shown to illustrate the half-unit-cell displacement induced by the Ruddlesden-Popper-type stacking faults (RP faults), resulting in the reduced cation contrast. **b**, Composite of the compressive strain measured on the [101] and [$\bar{1}$01] pseudocubic lattice fringes for the HAADF-STEM image in **a**. The infinite-layer film appears as a region of large compressive strain compared to the substrate because of the shortened *c*-axis lattice constant. Ruddlesden–Popper type faults in the film are highlighted as regions of local expansion (bright lines) within the film. The highlighted boundaries are used to annotate the vertical Ruddlesden–Popper regions, shown as black (yellow) boxes here (in Fig. 1a). **c**, Identical strain mapping of the [101] and [$\bar{1}$01] pseudocubic lattice fringes for the HAADF-STEM image of the $Nd_{0.85}Sr_{0.15}NiO_2$ film on LSAT substrate (Fig. 1b). The circles in **b** and **c** illustrate the coarsening length scale of the Fourier-based analysis. Scale bars, 5 nm.

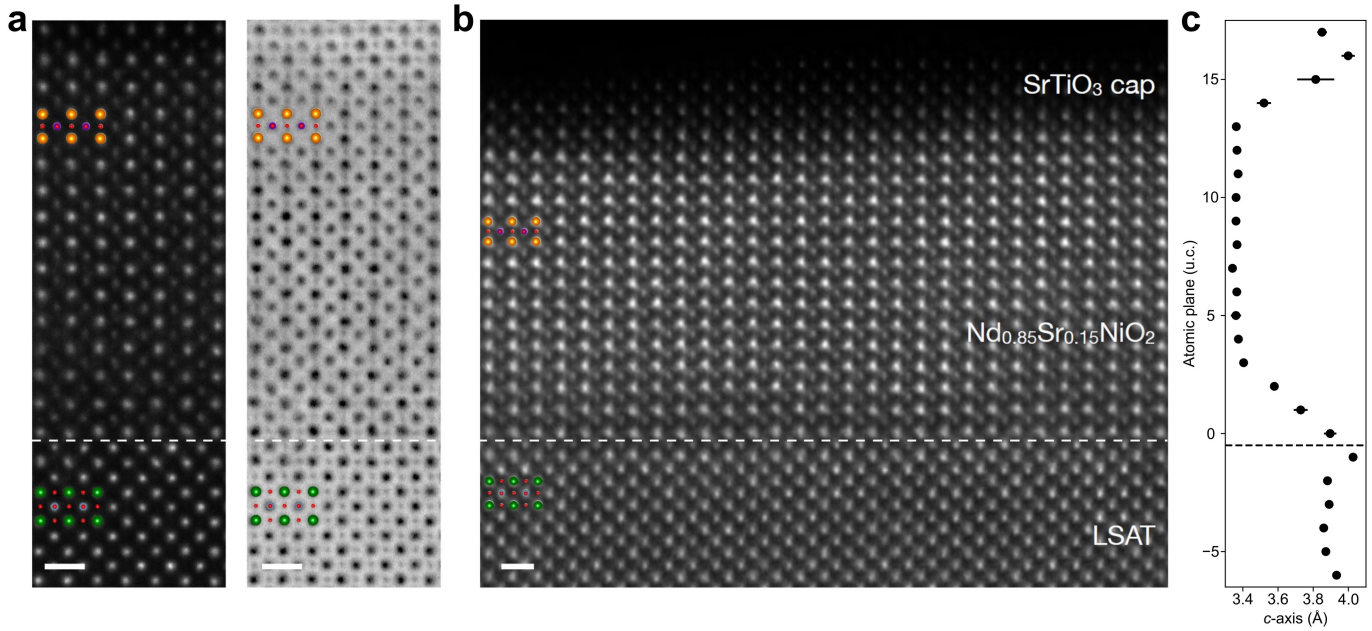

Extended Data Fig. 2 | High-resolution HAADF- and ABF-STEM imaging of $Nd_{0.85}Sr_{0.15}NiO_2$ film on LSAT. a, High-resolution HAADF- (left) and annular bright-field (ABF)- (right) STEM images of the $Nd_{0.85}Sr_{0.15}NiO_2$ film on LSAT shown in Fig. 1b. Both the lattice size and oxygen column structure visible in the ABF image are consistent with the infinite-layer structure. Atomic model overlays show columns of Nd/Sr (orange), Ni (purple), La/Sr (green), Al/Ta (blue), and O (red). **b**, HAADF-STEM image of the same $Nd_{0.85}Sr_{0.15}NiO_2$ film on LSAT. **c**. Quantitative tracking of the local *c*-axis lattice constant measured between consecutive A-site planes (e.g., Nd to Nd). The lattice constant within the film shows good agreement with the expected value for the infinite-layer structure and the measurements of a fully reduced film by XRD. Scale bars, 5 Å.

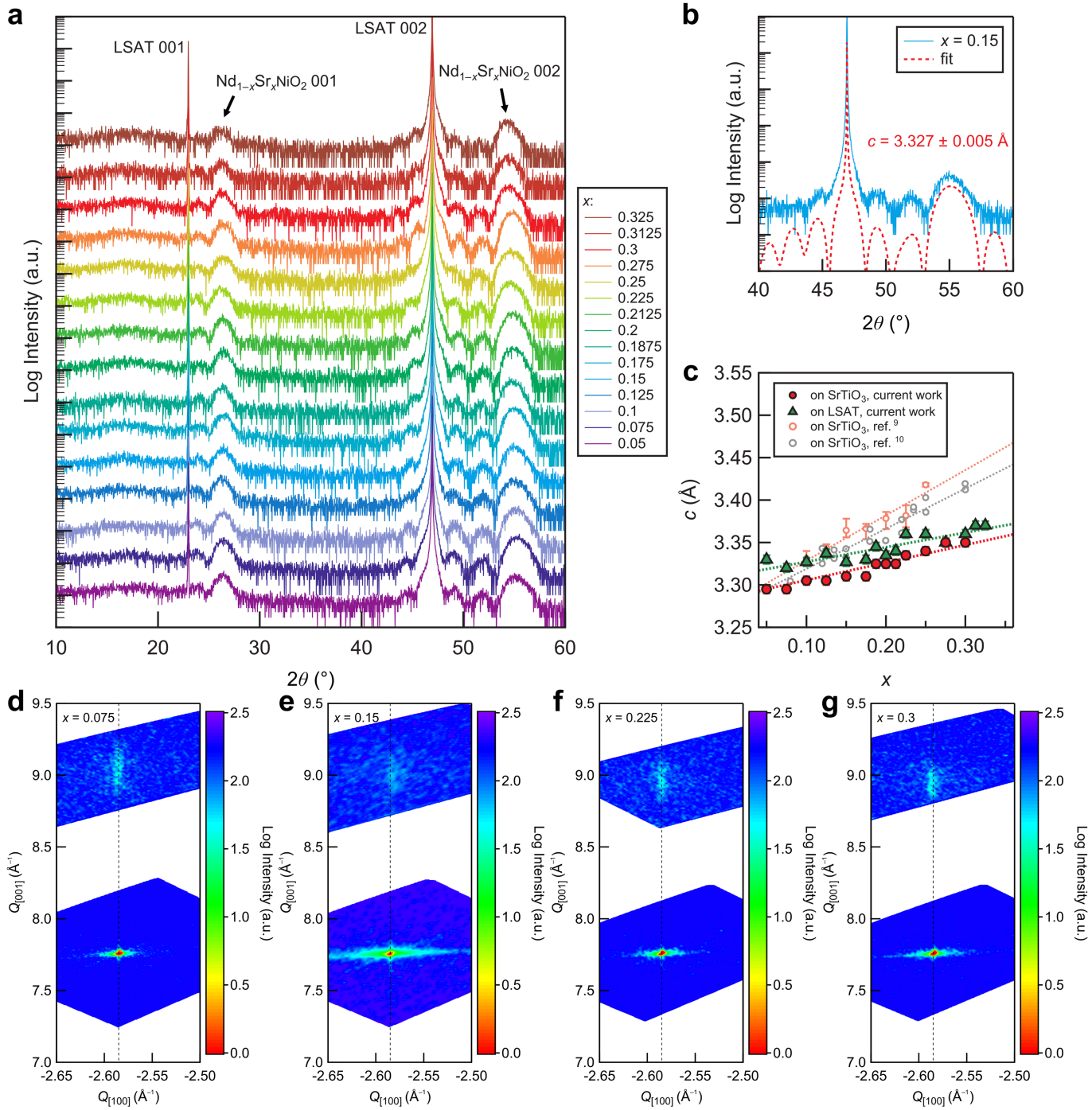

Extended Data Fig. 3 | X-Ray diffraction of $Nd_{1-x}Sr_xNiO_2$ on LSAT substrates. **a**, Representative XRD θ–2θ symmetric scans of optimized $Nd_{1-x}Sr_xNiO_2$ (x = 0.05–0.325). The curves are vertically offset for clarity. **b**, XRD θ–2θ symmetric scan of $Nd_{0.85}Sr_{0.15}NiO_2$ (solid curve) and the corresponding symmetric scan fit (dashed curve). The close agreement in the positions of the main film peak and the Laue fringes indicates a good fit. The asymmetry in the Laue fringes of the film peaks arises from the asymmetric background intensity and the resolution limit of the instrument. The extracted out-of-plane lattice constant c from the fit is labelled. **c**, c-axis lattice constant versus x for $Nd_{1-x}Sr_xNiO_2$ films on LSAT (green filled triangles, extracted from **a**) and on $SrTiO_3$ (red filled circles) using the same growth conditions (Extended Data Table 1). Error bars are the larger of the error in the fit and standard deviation in the values from multiple samples. c increases linearly with x, consistent with systematic doping of Sr in the films. Previous experimental data[9,10] on $SrTiO_3$ are also shown as open circles. The substantial elimination of Ruddlesden–Popper-type faults, which locally expand the in-plane lattice[11], results in the overall decrease in c compared to previous experimental data. In their absence, the larger c-axis lattice constant in LSAT with respect to $SrTiO_3$ is due to larger compressive strain. Dotted lines are linear fits to the experimental data. **d**–**g**, Reciprocal space maps of $Nd_{1-x}Sr_xNiO_2$ films on LSAT for x = 0.075 (**d**), x = 0.15 (**e**), x = 0.225 (**f**), and x = 0.3 (**g**), showing that the films are fully strained to the LSAT substrate across doping.

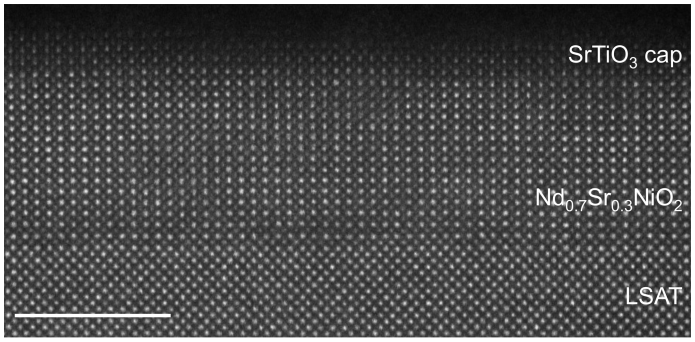

Extended Data Fig. 4 | Atomic-scale structural characterization by HAADF-STEM of the $Nd_{0.7}Sr_{0.3}NiO_2$ film on LSAT with $SrTiO_3$ capping layer. HAADF-STEM image of the $Nd_{0.7}Sr_{0.3}NiO_2$ film on LSAT. Scale bar, 5 nm.

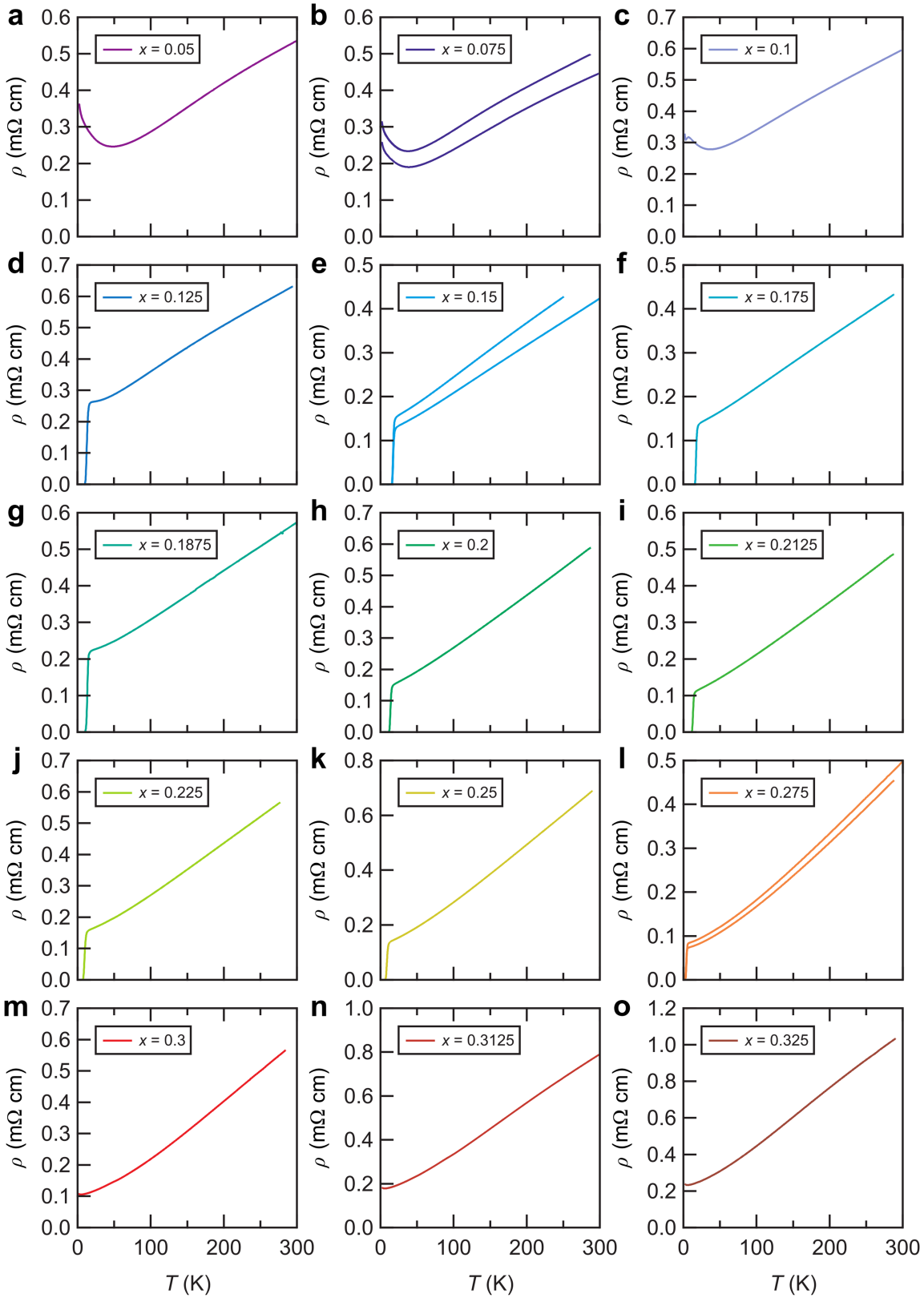

Extended Data Fig. 5 | Individual resistivity curves of $Nd_{1-x}Sr_xNiO_2$ on LSAT. ρ versus T curves of optimized $Nd_{1-x}Sr_xNiO_2$ films (x = 0.05–0.325). Curves for additional samples at x = 0.075, 0.15, and 0.275 are also shown.

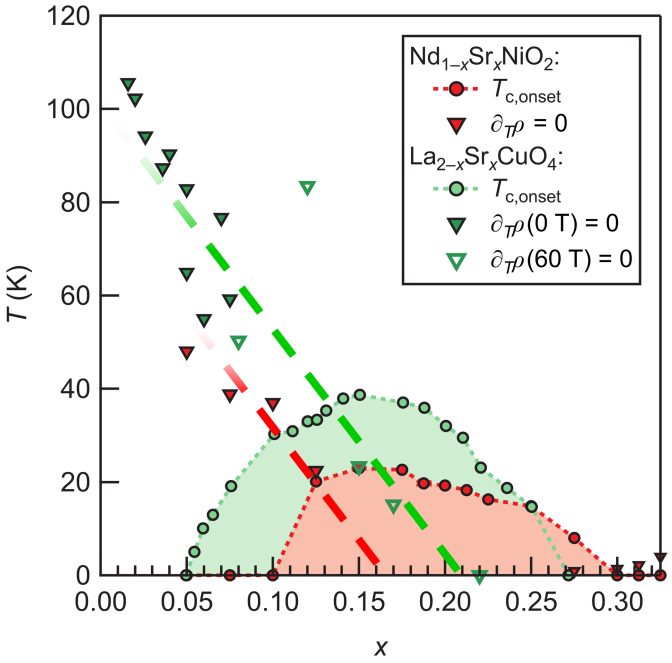

Extended Data Fig. 6 | Comparing the $Nd_{1-x}Sr_xNiO_2$ and the $La_{2-x}Sr_xCuO_4$ phase diagrams. Superconducting phase diagram of $Nd_{1-x}Sr_xNiO_2$ on LSAT (red) and $La_{2-x}Sr_xCuO_4$ (green), both plotted against the nominal Sr composition x[12,36,37,41]. The superconducting onset temperature is shown via circles, while the resistive upturn temperature T_{upturn} is shown as triangles. For $La_{2-x}Sr_xCuO_4$, the open triangles are T_{upturn} obtained by suppressing superconductivity with high magnetic field[37]. The superconducting dome extends from $x \approx 0.1$–0.3 ($\Delta x \approx 0.2$) for $Nd_{1-x}Sr_xNiO_2$ and $x \approx 0.05$–0.26 ($\Delta x \approx 0.21$) for $La_{2-x}Sr_xCuO_4$.

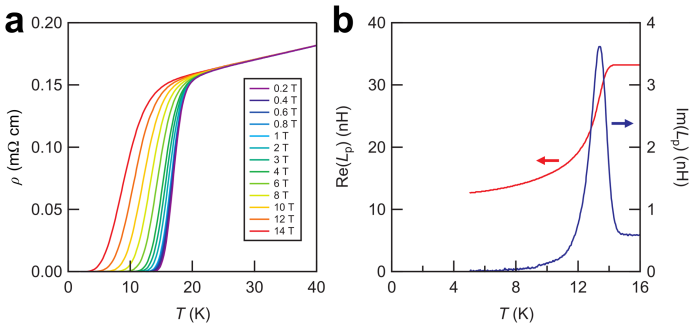

Extended Data Fig. 7 | Suppression of superconductivity by magnetic field. **a**, ρ versus T of $Nd_{0.825}Sr_{0.175}NiO_2$ film on LSAT under perpendicular magnetic field (0.2–14 T, indicated by color). **b**, The real (red, left) and imaginary (blue, right) parts of the inductance L_p as a function of T in the pickup coil on a $Nd_{0.825}Sr_{0.175}NiO_2$ film on LSAT, measured using a two-coil mutual-inductance measurement (see Methods).

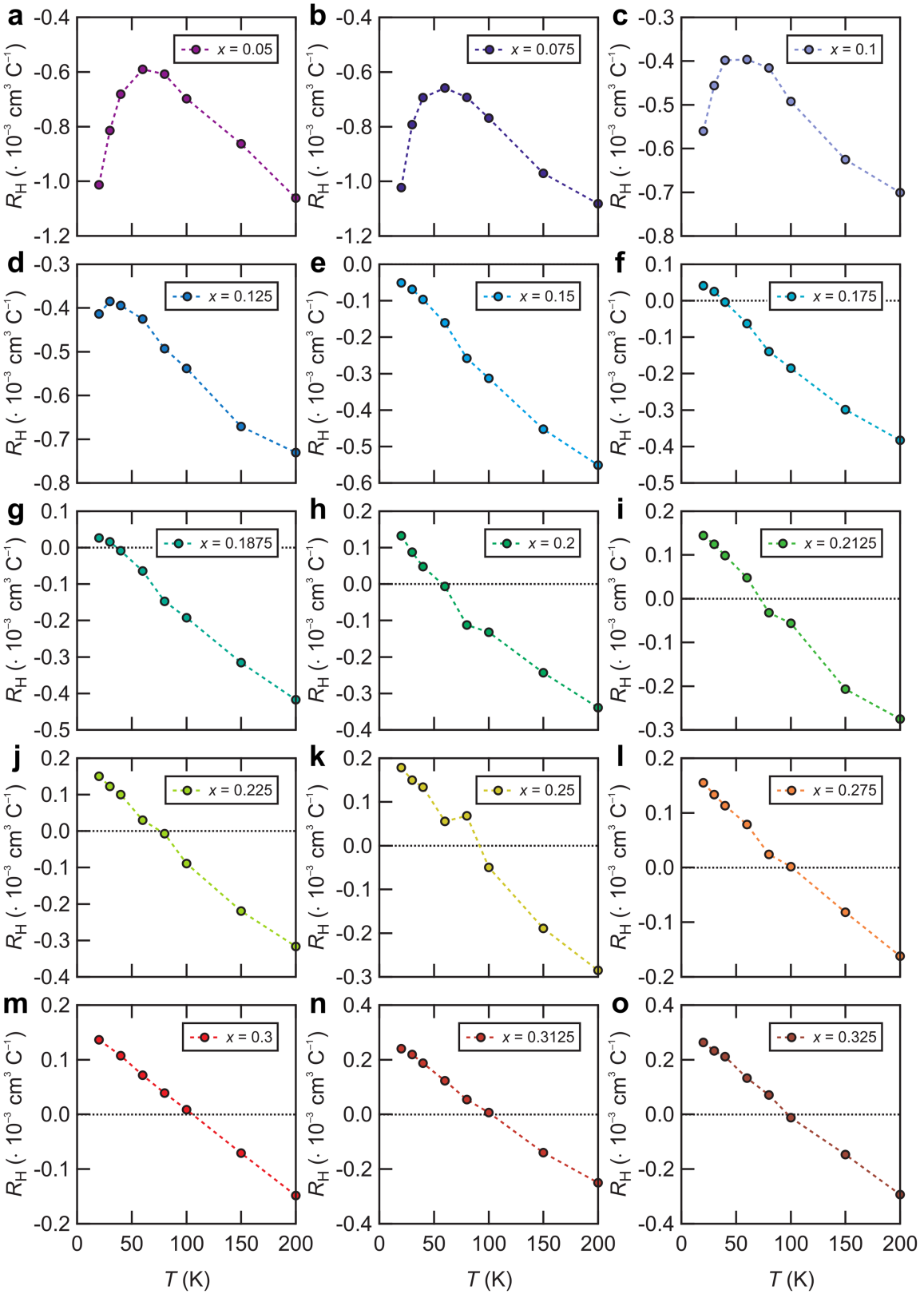

Extended Data Fig. 8 | Individual $R_H(T)$ curves of $Nd_{1-x}Sr_xNiO_2$ on LSAT. R_H versus T curves of optimized $Nd_{1-x}Sr_xNiO_2$ films (x = 0.05–0.325) on LSAT substrate. R_H = 0 is marked as a black dotted line.

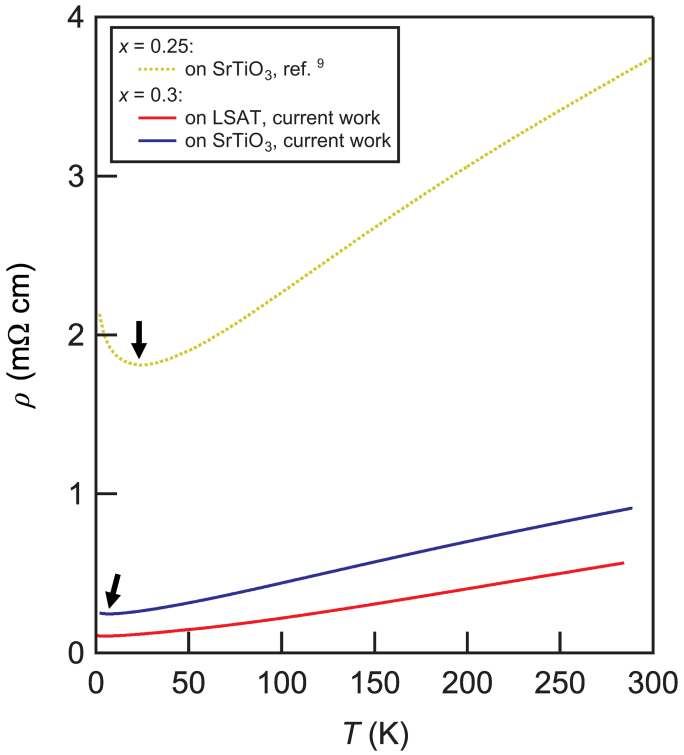

Extended Data Fig. 9 | Minimal epitaxial strain dependence of T_{upturn}. $\rho(T)$ of $Nd_{0.7}Sr_{0.3}NiO_2$ films on $SrTiO_3$ (blue) and LSAT (red), both synthesized using the growth parameters specified in Extended Data Table 1. Prior data of $\rho(T)$ of $Nd_{0.75}Sr_{0.25}NiO_2$ film on $SrTiO_3$ from ref. 9 (yellow dashed curve, see Fig. 2f) is also plotted for comparison. The films on $SrTiO_3$ show considerable suppression of T_{upturn} (black arrows) upon enhanced crystallinity, with similar order of suppression as the film on LSAT. This suggests that the suppression of the resistive upturn is primarily due to higher film quality, and epitaxial strain plays a sub-dominant role in the resistive upturn.

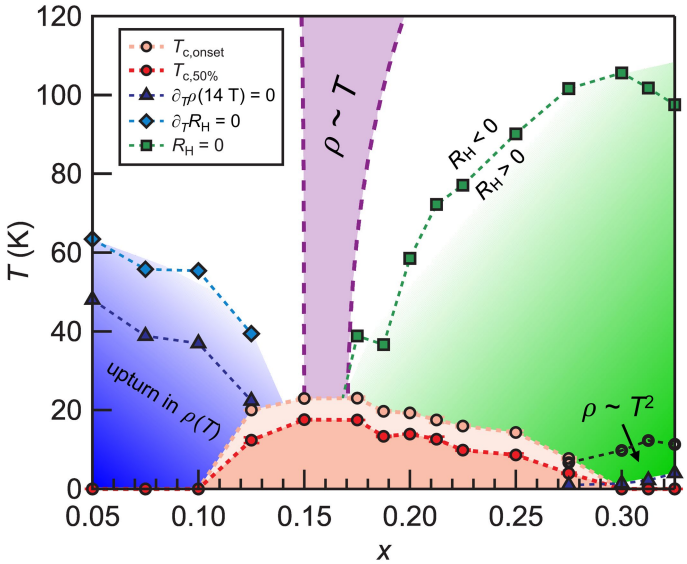

Extended Data Fig. 10 | Cumulative phase diagram of the infinite-layer nickelate $Nd_{1-x}Sr_xNiO_2$ on LSAT. The main features of the phase diagram of $Nd_{1-x}Sr_xNiO_2$ are summarized here. The onset temperature of the superconducting transition $T_{c,onset}$ is defined as the temperature at which the second derivative of $\rho(T)$ becomes negative, and the 50% transition temperature $T_{c,50\%}$ is defined as the temperature at which ρ is 50% of $\rho(T_{c,onset})$. In the underdoped region, ρ shows a resistive upturn, with T_{upturn} (dark-blue triangles) decreasing as hole doping is increased and superconductivity emerges. Simultaneously, the local maximum in R_H (light-blue diamonds) tracks the doping dependence of the resistive T_{upturn}. Superconductivity emerges at $x \approx 0.1$ and persists up to $x \approx 0.3$. In the optimal doping of $x \approx 0.15–0.175$, the normal-state resistivity shows a linear T-dependence. As superconductivity is suppressed in the overdoped region, T^2 resistivity emerges, with a small resistive upturn at low temperatures (dark-blue triangles) driven by disorder. The open circles at the overdoped region delineate the boundary below which the T^2 fit shows good agreement with ρ. As x is increased, R_H starts to cross zero into positive values (green squares). This transition occurs near the optimal doping, and the zero-crossing temperature increases into the overdoped region.

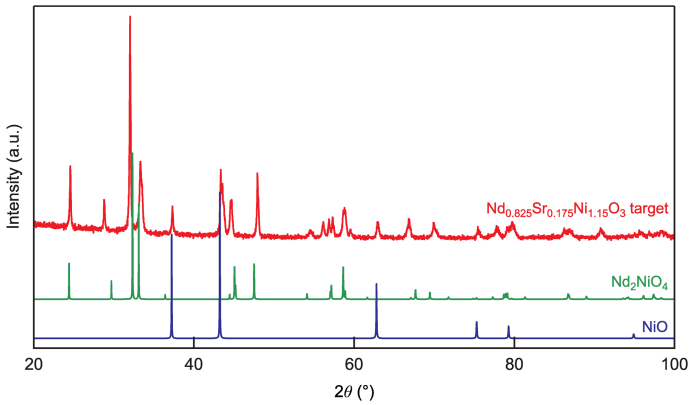

Extended Data Fig. 11 | Powder XRD of polycrystalline target. Powder XRD of polycrystalline nickelate target with nominal stoichiometry of $Nd_{0.825}Sr_{0.175}Ni_{1.15}O_3$ (red), along with bulk powder XRD of Nd_2NiO_4 and NiO[44,45]. Aside from minor shifts in the peak positions due to chemical substitution of Sr, the observed peaks of the target are a superposition of Nd_2NiO_4 and NiO[11].

Extended Data Table 1 | Pulsed-laser deposition growth parameters optimized for perovskite $Nd_{1-x}Sr_xNiO_3$ thin films on LSAT

Growth Parameters	Parameter Values
Fluence (J cm^{-2})	2.6
Laser spot size (mm^2)	0.77
Target composition	15% Ni rich
Pre-ablation pulse number	241
Target track outer diameter (cm)	1.0-1.1
Substrate-to-Target Distance (mm)	55.5
P_{O_2}, deposition (mTorr)	150
T, deposition (°C)	580

The optimized infinite-layer films were obtained across x by reducing the perovskite films at 240–260 °C for roughly 2.5–4 h (see Methods). We note that under the same reduction conditions, complete reduction could not be achieved for $x < 0.05$ on LSAT, and thus we limit our study to $x = 0.05–0.325$ (see Supplementary Information). For growth on $SrTiO_3$, the substrate was pre-annealed at 900 °C for 30 min at oxygen partial pressure $P_{O_2} = 5 \times 10^{-6}$ Torr.

Extended Data Table 2 | Summary of superconducting transition temperatures of $Nd_{1-x}Sr_xNiO_2$ thin films on LSAT

x	$T_{c,onset}$ (K)	$T_{c,90\%}$ (K)	$T_{c,50\%}$ (K)	$T_{c,10\%}$ (K)	$T_{c,0}$ (K)
0.125	20.1 ± 0.1	14.5 ± 0.6	12.4 ± 0.7	10.8 ± 0.7	6.9 ± 0.7
0.15	23.0 ± 0.1	19.2 ± 0.1	17.6 ± 0.1	16.5 ± 0.2	14.3 ± 0.2
0.175	23.0 ± 0.5	19.2 ± 0.1	17.5 ± 0.1	16.4 ± 0.2	14.1 ± 0.2
0.1875	19.7 ± 0.3	15.1 ± 0.3	13.3 ± 0.1	11.9 ± 0.1	8.5 ± 0.3
0.2	19.3 ± 0.1	15.7 ± 0.1	13.9 ± 0.1	12.8 ± 0.2	10.5 ± 0.3
0.2125	17.5 ± 0.7	14.2 ± 0.6	12.6 ± 0.6	11.5 ± 0.5	9.6 ± 0.6
0.225	16.0 ± 0.3	11.9 ± 0.1	9.8 ± 0.2	8.5 ± 0.2	6.2 ± 0.3
0.25	14.3 ± 0.5	10.5 ± 0.5	8.6 ± 0.4	7.2 ± 0.5	4.8 ± 0.2
0.275	7.7 ± 0.3	5.1 ± 0.3	4.0 ± 0.2	3.0 ± 0.2	< 2

The onset temperature of the superconducting transition $T_{c,onset}$ is defined as the temperature at which the second derivative of $\rho(T)$ becomes negative. The 90%, 50%, and 10% transition temperatures ($T_{c,90\%}$, $T_{c,50\%}$, and $T_{c,10\%}$, respectively) are defined as the temperatures at which ρ is 90%, 50%, and 10% of $\rho(T_{c,onset})$, respectively. $T_{c,0}$ is the temperature at which $\rho=0$.